Vortex-induced type III planetary migration

M-K. Lin

mkl23@cam.ac.uk

DAMTP, Cambridge University

ABSTRACT

We present studies of the interaction of a Saturn-mass planet with a massive gaseous disc. In this regime of planet and disc mass, the planet can change its orbital semi-major axis due to the exchange of angular momentum with material that crosses the planet's orbital radius. This is commonly known as type III or runaway migration. We focus on low viscosity discs. We show that thin vortensity rings form as a result of shocks induced by the planet potential, and the shocks extend close to the planet's orbital radius. The stability of such vortensity rings is analysed and found to be dynamically unstable. The unstable modes are focused around vortensity (the curl of the disc's velocity field divided by its surface density) minima. Numerical simulations show they develop into large-scale vortices in the non-linear regime. These vortices are found to scatter the planet inwards, resulting in non-smooth type III migration in low viscosity discs.

1. Introduction

The importance of planetary migration, whereby a planet changes its separation from its host star, was realised with the discovery of the first extrasolar planet 51 Pegasis b (Mayor & Queloz 1995) with an orbital period of 4 days. Such planets, classified as 'hot Jupiters' orbit so close to their host stars it is difficult to model their formation in situ. It is thought they form further out then migrate inwards due to disc torques. Tidal interactions between a planet and protoplanetary disc have been studied well before observations and generally leads to orbital decay of the planet's semi-major axis (Goldreich & Tremaine 1979, 1980). These early studies focused on what is now refereed to as type I migration (Ward 1997) where the planet is treated as a small perturbation to the disc, and its response calculated by solving the linearised hydrodynamic equations that govern disc evolution. If the planet mass is large, comparable to Jupiter, linear theory ceases to apply and we enter type II migration Lin & Papaloizou (1986). Here, the planet opens a density gap in the disc, and drifts towards the central star along with the disc material, which is undergoing viscous evolution.

Type I and type II have been extensively discussed in literature, the distinction usually taken as whether or not the planet opens a gap. However, for intermediate mass planets comparable to

Saturn, a partial gap is opened. If the planet migrates there is a torque associated with disc material flowing across the planet's orbital radius (described below). This relatively recently discovered migration mode is termed type III migration (Masset & Papaloizou 2003). It has been further discussed by Artymowicz (2004a); Papaloizou (2005) and a series of detailed numerical studies was presented by Pepliński et al. (2008a,b,c).

In this essay we shall be concerned with low viscosity or inviscid discs. These discs exhibit dynamical instabilities associated with steep gradients in the disc (Papaloizou & Pringle 1984; Papaloizou & Lin 1989; Lovelace et al. 1999; Li et al. 2000) and vortices develop in the non-linear regime (Li et al. 2001). This is applicable to protoplanetary discs where steep gradients is associated with gap edges and de Val-Borro et al. (2007) showed the formation of large-scale vortices at gap edges of a Jupiter-mass planet held on fixed circular orbit. The migrating case was considered by Ou et al. (2007) for a Neptune-mass planet. In this paper we examine this effect in more detail for a Saturn mass planet undergoing type III migration.

This essay is organised as follows. We first briefly review the basic physical concepts of type III migration next. In §2 we introduce our numerical model and methods. In §3 we present numerical simulations of type III migration as a function of viscosity, focusing on low viscosity discs. We shall find that migration is non-smooth due to instabilities in the disc. In §4 we explain the formation of the unstable basic state and perform linear analysis stability in §5. We then apply results from linear theory to vortex-induced migration in §6. Finally §7 concludes this essay.

1.1. Physics of type III migration

Let us consider the flow topology of a Saturn-mass planet in a gaseous disc, both orbiting a central star. The flow near the planet is shown schematically in Fig. 1. The flow is divided into the horse-shoe region (red) of width $2x_s$, where material trapped on horse-shoe orbits; and the circulating region where fluid elements complete circular orbits around the entire disc (blue). There is also material that circulates the planet, inside its Roche or Hill radius (see below). Now, let the planet move inwards at a rate $\dot{a} < 0$. a is the planet's semi-major axis, which is close to the planet's instantaneous orbital radius $r_p(t)$ since its orbit is nearly circular. Disc material can cross from the inner disc (blue) to the outer disc by executing one horse-shoe turn behind the planet, but when it returns from the top, the planet has moved inwards (thin-solid black arrow). The fluid element has changed orbital radius $a - x_s \to a + x_s$, gaining angular momentum and therefore exerts a negative torque on the planet:

$$\Gamma_3 = 2\pi a^2 \dot{a} \Sigma_e \Omega(a) x_s, \tag{1}$$

where Σ_e is the density at the upstream separatrix (see Fig. 1), $\Omega(a)$ is the fluid angular speed at orbital radius of a (which is close to the planet's angular speed) and x_s is half the horse-shoe width. Appendix A shows in the zero-pressure limit $x_s \lesssim 2.3 r_h$, where $r_h = (M_p/3M_*)^{1/3} r_p$ is the Hill radius within which the gravity of the planet, mass M_p, dominates that over the central star

of mass M_*. In the hydrodynamic limit it has been measured to be $x_s \simeq 2.5r_h$ (Artymowicz 2004b; Paardekooper & Papaloizou 2009), which will be taken for later results analysis.

The migrating mass includes the planet, fluid inside the planet's Roche lobe M_r and fluid trapped in horse-shoe orbits $M_h = 4\pi\Sigma_g a x_s$. The migration rate is then
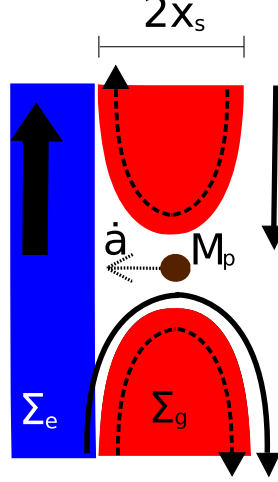

Fig. 1.—: Illustration of inwards type III migration. Fluid crossing from the inner disc to outer disc executes one horse-shoe turn behind the planet. The fluid gains angular momentum which exerts a negative torque on the planet, encouraging further orbital decay.

$$\dot{a} = \frac{2\Gamma_{\mathrm{L}}}{\Omega(a)a(\underbrace{M_p + M_{\mathrm{r}}}_{M_p'} - \delta m)} \qquad (2)$$

where Γ_L is the total Lindblad torque (which would be the main contributor to type I migration) and

$$\begin{aligned} \delta m &= 4\pi\Sigma_e a x_s - M_h \\ &= 4\pi a x_s(\Sigma_e - \Sigma_g) \end{aligned} \qquad (3)$$

is the density-defined co-orbital mass deficit. Eq. 2 imply migration speed increases with δm. The simplified description above follows Papaloizou et al. (2007a). Qualitatively, since the horse-shoe material is assumed to move with the planet, it adds inertia to the migrating system and the orbit-crossing material provides the torque to move the system. Hence, the more 'fuel' (Σ_e) there is relative to the inertia (Σ_g), the faster the migration.

Processes that contribute to Σ_e) favours migration while processes contributing to the gap term (e.g. Σ_g) slows migration. It is conceivable that instabilities associated with gap edges increases Σ_e and hence δm, thereby encouraging type III or runaway migration.

2. Basic model and governing equations

We consider a planet of mass M_p orbiting a central star in a thin disc and use polar co-ordinates (r, ϕ) centred on the primary in a non-rotating frame (unless otherwise stated). Units are such that the gravitational constant $G = 1$, central star mass $M_* = 1$ and the initial orbital radius of the planet is $r_p t = 0 = 2$. The unit of time is then $P_0 = 2\pi/\Omega_p$ where $\Omega_p = \sqrt{GM_*/r_p^3(0)}$ is the initial orbital speed. The disc is governed by the two-dimensional hydrodynamic equations

$$\frac{\partial \Sigma}{\partial t} + \nabla \cdot (\Sigma \mathbf{v}) = 0, \tag{4}$$

$$\frac{\partial v_r}{\partial t} + \mathbf{v} \cdot \nabla v_r - \frac{v_\phi^2}{r} = -\frac{1}{\Sigma}\frac{\partial P}{\partial r} - \frac{\partial \Phi}{\partial r} + \frac{f_r}{\Sigma}, \tag{5}$$

$$\frac{\partial v_\phi}{\partial t} + \mathbf{v} \cdot \nabla v_\phi + \frac{v_\phi v_r}{r} = -\frac{1}{\Sigma r}\frac{\partial P}{\partial \phi} - \frac{1}{r}\frac{\partial \Phi}{\partial \phi} + \frac{f_r}{\Sigma}, \tag{6}$$

where Σ is the disc surface density, $\mathbf{v} = (v_r, v_\phi)$ is the fluid velocity and P is the vertically integrated pressure give by a locally isothermal equation of state

$$P = c_s^2(r)\Sigma. \tag{7}$$

The sound speed is $c_s = hv_k$ where $h = H/r$ is the constant aspect ratio, H being the disc semi-thickness, and $v_k = r^{-1/2}$ is the Keplerian azimuthal speed. Φ is the total potential including primary, planet (with softening length $\epsilon = 0.6H$) and indirect terms. Disc self-gravity is not included in the calculation. f_r and f_ϕ are viscous forces proportional to the uniform kinematic viscosity $\nu = \nu_0 \times 10^{-5}$, in physical units of $r_p^2(0)\Omega_p$. Details of the two source terms can be found in Masset (2002).

Parts of this essay employs the 'vortensity', η, to describe disc evolution. It is defined as

$$\eta = \frac{\omega}{\Sigma} \equiv \frac{\omega_r + 2\Omega_p}{\Sigma}, \tag{8}$$

where $\omega_r = \hat{\mathbf{z}} \cdot \nabla \wedge \mathbf{v}$ is the relative vorticity seen in a frame that rotates with the planet. In barotropic flows without shocks, vortensity is conserved following a fluid particle. When non-barotropic equation of state (Eq. 7) is used, vortensity conservation is still a good approximation locally as long as there are no shocks, because the sound speed varies on a global scale. η is an important quantity because it determines the disc stability and the formation and evolution is also clearer when viewing the vortensity. Also, η^{-1} was used by Masset & Papaloizou (2003) to define the co-orbital mass deficit δm by comparing η^{-1} at the gap edge and that within the gap. It served the same role as Σ_e and Σ_g in Eq. 3.

We use the FARGO code to evolve the system (Masset 2000a,b). The hydrodynamic part is solved using a finite-difference scheme with van Leer upwind The disc is divided on a grid, into $N_r \times N_\phi$ sectors in the radial and azimuthal directions, respectively. FARGO is similar to the ZEUS code (Stone & Norman 1992) but it employs a modified algorithm for azimuthal transport that allows for large time steps. We take 2π-periodic boundary condition in the azimuth and wave

damping boundary conditions at disc boundaries (de Val-Borro 2006). The planet moves under the disc, primary and indirect potentials and its motion integrated with a 5th order Runge-Kutta method.

3. Type III migration as a function of viscosity

We illustrate type III migration and consider the effect of lowering viscosity. The disc extends $r = [0.4, 4.0]$ and is initialised with uniform density $\Sigma = \Sigma_0 \times 10^{-4}$, azimuthal velocity $v_\phi = v_k\sqrt{1 - h^2}$ and radial velocity $v_r = -3\nu_0 \times 10^{-5}/2r$. The aspect ratio is uniform $h = 0.05$. The planet has fixed mass $M_p = 2.8 \times 10^{-4}$, corresponding to Saturn if M_* is the Solar mass. The full planet potential is applied from $t = 0$. We choose $\Sigma_0 = 7.0$ as a fiducial value. The computational domain has $N_r \times N_\phi = 768 \times 2304$ grids, giving a resolution of $0.05r_h$ and $0.06r_h$ in radius and azimuth, respectively, at $r = 2$.

Fig. 2 shows migration $a(t)$ as a function of viscosity ν_0. Standard viscosity $\nu_0 = 1$ yields characteristic orbital decay in less than $100P_0$, implying self-sustained type III migration (Masset & Papaloizou 2003; Papaloizou et al. 2007b; Pepliński et al. 2008b). $a(t)$ is indistinguishable for $0 < t \lesssim 15$ because viscous time-scales are much longer than dynamical time-scales. Migration is initially inwards (the total Lindblad torque being typically negative) and relatively slow. Low viscosity discs experience brief episodes of rapid migration where its semi-major axis 'jumps' a few Hill radii inwards and the deceleration at $r = 1.4$ is independent of ν_0. For $\nu_0 = 1.0, 0.5$ migration proceeds across smoothly, slowing down towards the end, signifying end of type III migration. Lowering ν_0 amplifies the 'kink', particularly in the inviscid limit, migration stalls temporarily and re-starts.

Despite differences in detail, the extent of orbital decay between viscous and inviscid disc is similar. This is not surprising under type III migration because torque is due to fluid material crossing the planet's orbital radius. The extend of orbital decay should not depend on the nature of this flow but only on the amount of disc material participating in the interaction. Since the disc mass inside r_p is the same for all ν, we do not expect significant difference between inviscid/viscous discs overall. However, if the flow across r_p is not a smooth function of time, then migration would be non-smooth as observed in Fig. 2. The result here already suggest that lowering the viscosity makes this flow-through non-smooth.

3.1. The connection between vortensity and migration

Masset & Papaloizou (2003) defines the co-orbital mass deficit through $\eta^{-1} = \Sigma/\omega$. Assuming the planet is on Keplerian orbit, their definition can be simplified to the form

$$\delta m = 2\pi x_s r_p^{-1/2}(\langle \Sigma/\omega \rangle_{\text{circ}} - \langle \Sigma/\omega \rangle_{\text{coorb}}), \tag{9}$$
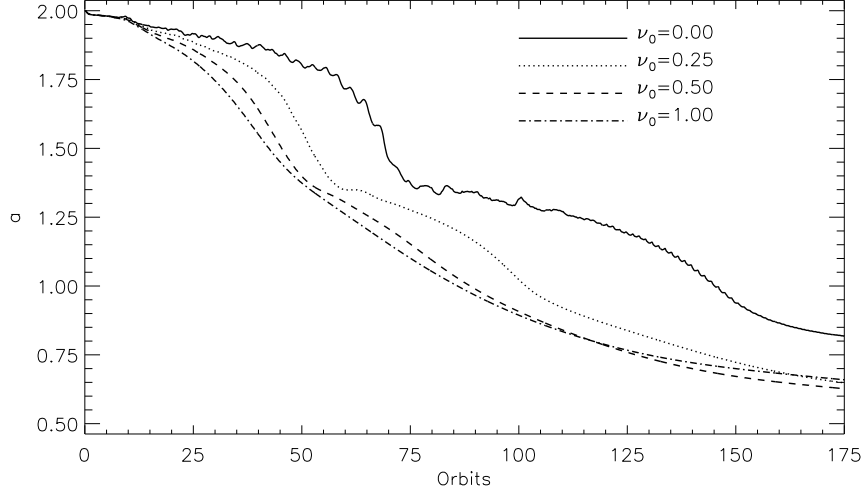
Fig. 2.—: Effect of uniform kinematic viscosity on migration.

which compares η^{-1} in circulating and co-orbital fluid. Hence, η^{-1} is an useful diagnostic to explain migration curves (Fig. 2). Note that Eq. 9 reduces to Eq. 3 if one neglects variation in vorticity ω in the region of interest.

Fig. 3 shows the azimuthally averaged Σ/ω-perturbation following the planet. Introducing the planet produces low-Σ/ω (high vortensity) rings at $r - r_p \simeq \pm 2r_h$ within $t \lesssim 10$ (Fig. 3(a)). A horse-shoe width of $x_s = 2.5r_h$ means they are co-orbital features, unlike vortensity rings produced by low mass planets which occur in the circulating region (e.g. Koller et al. 2003; Li et al. 2005). Increasing ν reduces the ring amplitudes, but their locations are unaffected. Ring-formation is not sensitive to ν because they form on dynamical time-scales which is much shorter than viscous time-scales. Viscosity takes effect by $t = 50$ (Fig. 3(b)), producing much smoother profiles for $\nu_0 = 0.5, 1.0$. Following the planet, the perturbed profile can appear to be smoothed if the planet migrates through the background (which is $\Sigma/\omega \propto r^{3/2}$) and *not* carrying its gap structure, i.e. loss of horse-shoe material. This has been confirmed by examining the evolution of a passive scalar initially placed in the co-orbital region, and later lost.

In Fig. 3(b) only the inviscid disc retains the inner ring of low Σ/ω, and only this case has not yet gone into rapid migration (Fig. 2). This suggests vortensity rings present a structural obstacle to flow of material across the planet's orbital radius. At $t = 65$ (Fig. 3(c)) the $\nu_0 = 0.5, 1.0$ cases have qualitatively unchanged profiles. For $\nu_0 = 0.25$, migration speed has lowered with the re-formation of vortensity double-rings after a stalling at $t \sim 60$ (Fig. 2), The peaks and troughs of

Σ/ω are close to those in the initial phase (Fig. 3(a)), implying migration can experience repeated episodes. The inviscid case is now in rapid migration and note the loss of the inner vortensity ring.

Fig. 3(d) show the final profile. Viscous cases are in slow migration, and have much smoother profiles. The inviscid disc retains the double-ring/gap structure, but is also in slow migration. This indicates two possible co-orbital configurations to slow type III migration.
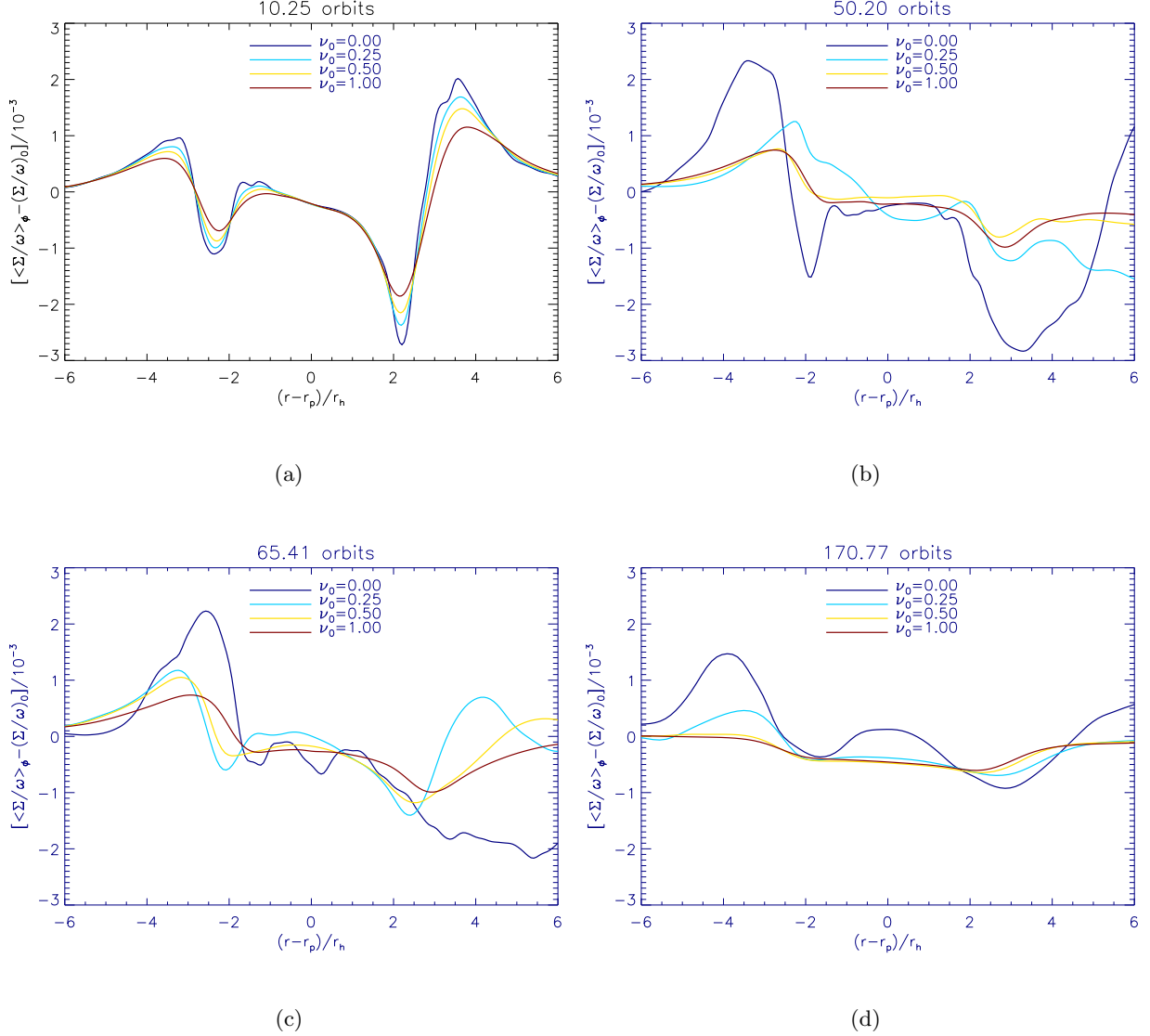

Fig. 3.—: Σ/ω-perturbation for different viscosities for the standard case $\Sigma_0 = 7$, $M_p = 2.8 \times 10^{-4}$. Here we use $\omega = r^{-1}\partial_r(rv_\phi)$ to represent vorticity rather than its full expression involving $\partial v_r/\partial\phi$. This is valid since $|v_r| \ll |v_\phi|$.

3.2. The inviscid disc

The simple experiments above show that low viscosity produces non-smooth migration and that type III migration is correlated with co-orbital structure. We now focus on the inviscid disc in more detail in order to understand these effects. The key times in its migration history(Fig. 2) are : $t \lesssim 45$ (slow migration); $60 \lesssim t \lesssim 70$ (rapid migration); $t \sim 75$ (stopping) and $75 \lesssim t \lesssim 110$ (slow migration). Average migration rates are, respectively, $\dot{a}(25) \sim -3 \times 10^{-3}$; $\dot{a}(65) \sim -2 \times 10^{-2}$ and $\dot{a}(85) \sim -2 \times 10^{-3}$.

These phases correspond to different disc structures. Fig. 4 shows global density evolution. During slow migration at $t = 24.75$, the planet resides in a partial gap ($|r - r_p| \lesssim 2.3 r_h$) with density $\sim 20\%$ lower than Σ_0. The circular gap is non-axisymmetric with a low density arc just inside the outer gap edge. More importantly are large-scale vortices (or over-densities) just outside gap edges centred at $(-0.3, -1.5)$ and $(0.5, 2.4)$ respectively, both of azimuthal extent $\Delta\phi \sim \pi$. The outer (inner) vortex rotate clockwise (counter-clockwise) relative to the planet. Here, we shall focus on their effects on migration, and explore their origin later.

At $t = 65.05$ in Fig. 4, the planet is just inside the inner gap edge. Front-back density contrast is largest as inner vortex enters the co-orbital region from behind. It exerts a negative torque as vortex material crosses to the exterior disc, hence this snapshot corresponds to rapid migration. At $t = 75$ the planet no longer resides inside a gap. Compared to $t = 25$, the planet has effectively left its gap by scattering vortex outwards. This completes a single episode of vortex-planet interaction. In this inviscid case, migration stalls temporarily. The outer vortex simply circulates the previous outer gap edge and does not influence co-orbital dynamics.

In order to show that it is a material volume of fluid that interacts with the planet, we show in Fig. 5 the evolution of inverse vortensity Σ/ω and recall that in this inviscid disc, Σ/ω is approximately conserved following a fluid element, except across shocks. By 25 orbits, vortensity rings of widths $O(H)$ $(= O(r_h))$ form just inside gap edges, outlining material trapped in horse-shoe orbits. Their formation through shocks will be discussed in the next section. Steep gradients associated with these rings lead non-axisymmetric instabilities which develop into vortices in the non-linear regime. At $t = 55$ the inner vortex begins to interact with co-orbital region. Vortensity conservation imply red blobs near the outer ring was part of the inner vortex, During rapid migration at $t = 65$, the main vortex body flows across co-orbital region. The inner ring is strongly disrupted and co-orbital region no longer well-defined. This contrasts the standard type III migration scenario where material simply transfers from inner to outer disc leaving co-orbital region unaffected (e.g. Masset & Papaloizou 2003). However, in the inviscid disc, disruption is *necessary* due to vortensity rings of much higher vortensity than the vortex. Type III migration under vortensity conservation means the vortex must cross the planet orbit without changing vortensity. This is impossible if one simultaneously impose the ring structure (since ring material is co-orbital). Intense vortensity rings inhibits the flow-through and type III migration only becomes significant with ring disruption.

When migration stalls at $t = 75$, Fig. 5 show vortensity rings are much less pronounced
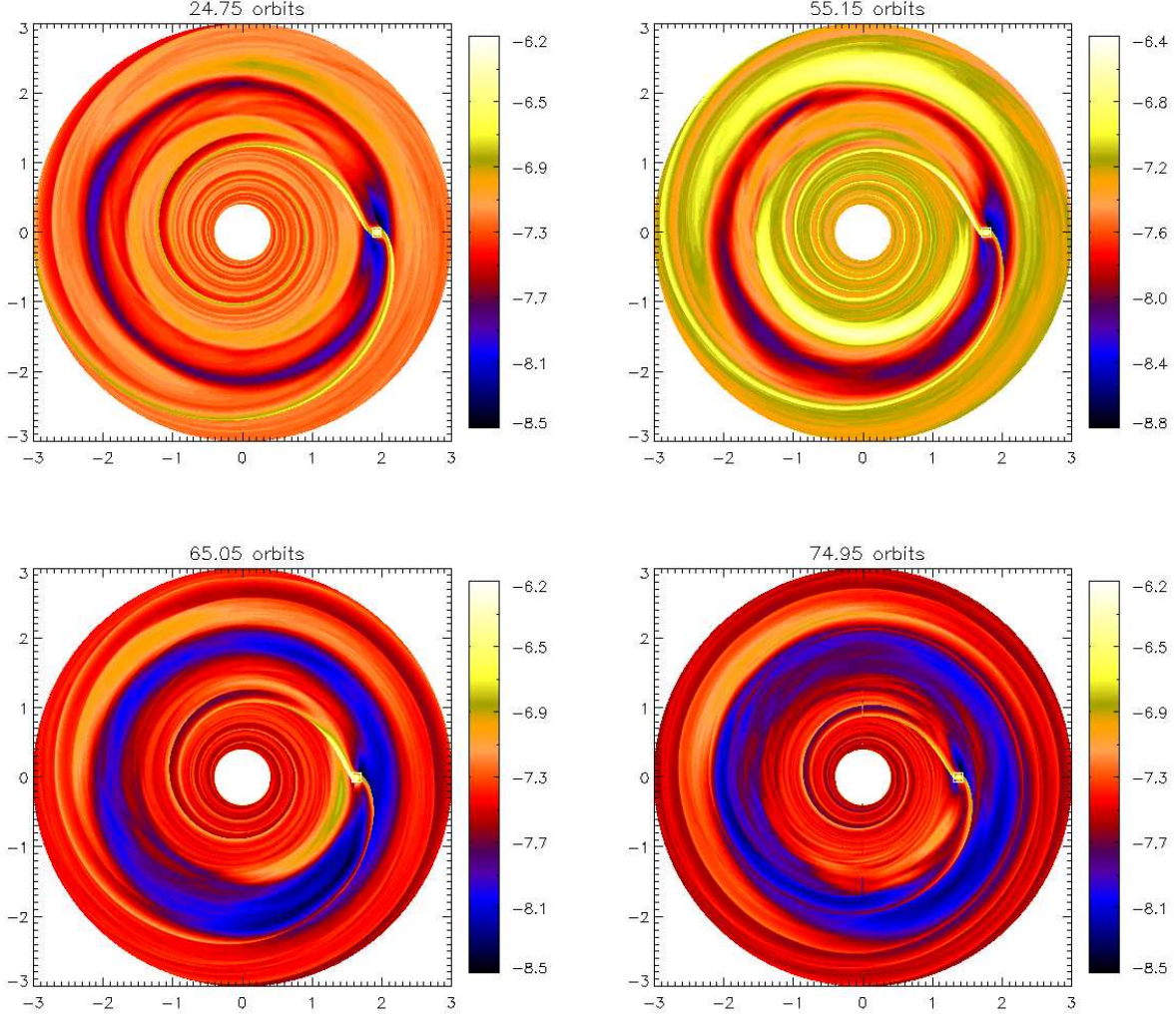
Fig. 4.—: $\ln \Sigma$ from early slow migration to first stopping (~ 75 orbits).

compared to initial phase. At the planet's new position, high-Σ/ω material fills the new co-orbital region, lowering the co-orbital mass deficit δm. The vortex ahead of planet also remove front-back asymmetry. It is clear from this figure that type III migration cannot continue because there is no more material to continue to cross r_p from the inner disc. Vortensity rings re-form by $t = 85$. The vortex material which passed to the outer disc during the first rapid migration phase is now irrelevant, much like the outermost vortex. Note also at $t = 100$, there is one vortex associated with inner gap edge and two associated with the outer ring. This is simply a repeat to the build up of the first episode of rapid migration. This vortex induces another phase of rapid migration later on, but with less abrupt jump in orbital radius.
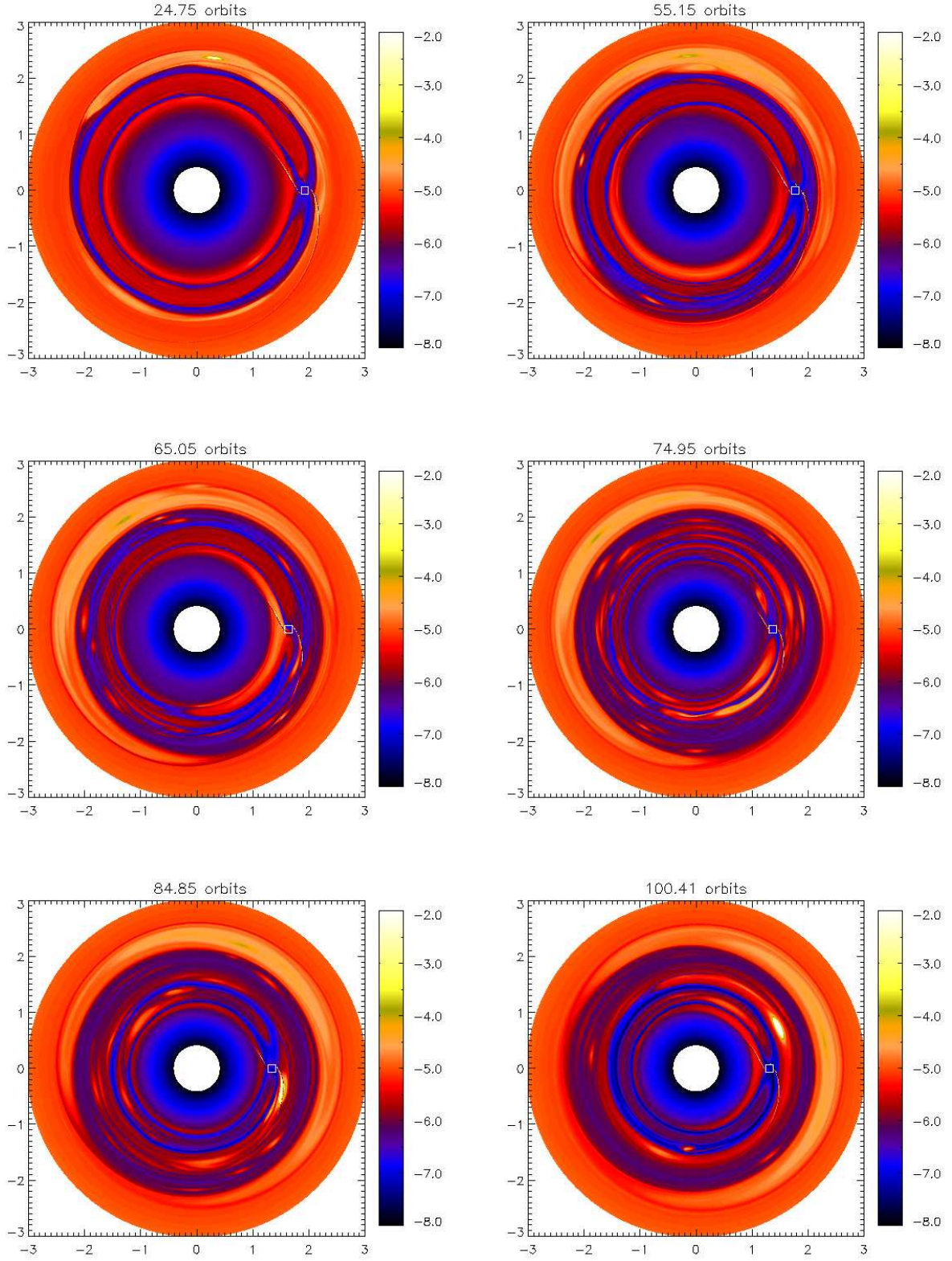
Fig. 5.—: $\ln \Sigma/\omega$ from early slow migration to sudden stopping (~ 75 orbits) to second phase slow migration.

4.   Vortensity rings in the limit of zero viscosity

The previous section illustrated the association of vortensity rings and migration. Vortices form adjacent to these rings and are responsible for fast migration episodes. This section studies their formation process. We first use hydrodynamic simulations to show vortensity rings originate from shocks near a Saturn-mass planet. We then construct a semi-analytic model to predict the vortensity generation from first principles. Our modelling confirm vortensity generation within a planet's co-orbital region, thereby modifying co-orbital properties.

4.1.   Hydrodynamic simulations

The setup is largely the same as above, except for the following modifications. The computation domain is now $r = [1, 3]$ and initial uniform density $\Sigma = 10^{-4}$. The planet is now held on fixed circular orbit at $r_p = 2$ with Keplerian speed $\Omega_p = r_p^{-3/2}$. Its potential is switched on over 5 orbits. The disc is relatively narrow in radial extent in order to increase resolution which was chosen at $N_r \times N_\phi = 1024 \times 3072$, or $\Delta r \simeq 0.02 r_h$ radially and $r\Delta\phi \simeq 0.05 r_h$. We shall observe that ring formation is due to shocks near the plant and therefore independent of boundary conditions. As long as boundary conditions do not allow wave-reflection, co-orbital dynamics should be unaffected.

Fig.6 shows the vortensity field at $t = 7.07$ close to the planet. Vortensity is generated/destroyed across the two spiral shocks. For the outer shock, vortensity generation occur in fluid elements executing a horse-shoe turn and vortensity destroyed in circulating fluid but the change is smaller in magnitude. The situation is similar for the inner shock, although some post-shock material continue to circulate. However, it is clear from Fig. 6 most vortensity generation is through horse-shoe turns.

Vortensity is generated along a length $l \sim r_h \sim H$, resulting in thin rings on the same radial scale, which eventually goes around the disc and outlines the entire co-orbital region. Their origin from horse-shoe turns enhance the contrast between circulating and co-orbital regions. For example: outer disc horse-shoe material is mapped $r + x \rightarrow r - x$ and increases vortensity as it crosses the shock. It is put adjacent to circulating inner disc material, which decreases in vortensity post-shock. It is then natural to question the stability of this configuration, which will be addressed later. First, let us attempt to model the process of shock-generation of vortensity.

4.2.   Predicting the vortensity generation

We specifically model vortensity generation across the outer spiral shock in Fig. 6. We require: vortensity jump condition, the pre-shock flow field and shock front. We describe each component in turn.
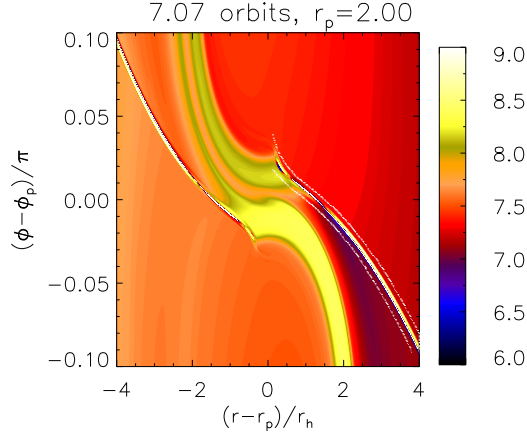
Fig. 6.—: Vortensity generation and destruction across shocks induced by a Saturn-mass planet in an inviscid disc. The plot shows ω/Σ on a logarithmic scale. Vortensity can be negative inside the shock and is not plotted. Data at white lines are interpreted as pre- and post-shock.

4.2.1. Vorticity and vortensity jumps

The jump in absolute vorticity $[\omega]$ is readily obtained by resolving the fluid motion parallel and perpendicular to the shock front Kevlahan (1997). As we do not solve the energy equation, shocks are isothermal and a brief derivation of $[\omega]$ is presented in the Appendix B. The result for a steady shock is

$$[\omega] = -\frac{(M^2-1)^2}{M^2}\frac{\partial v_\perp}{\partial S} + (M^2-1)\omega - \left(\frac{M^2-1}{v_\perp}\right)\frac{\partial c_s^2}{\partial S}, \tag{10}$$

where $v_\perp$ is the velocity perpendicular to the shock, $M = v_\perp/c_s$ is perpendicular Mach number. $\partial/\partial S$ is derivative along the shock, defined to correspond to increasing r. The local isothermal equation of state produces the bacroclinic term on RHS of Eq. 10, which differs to the expression in Kevlahan (1997) for adiabatic shocks and Li et al. (2005) for global isothermal equation of state. Its contribution is not significant here, because vortensity generation is local.

The vortensity jump $[\omega/\Sigma]$ follows immediately from Eq. 10,

$$\left[\frac{\omega}{\Sigma}\right] = -\frac{(M^2-1)^2}{\Sigma M^4}\frac{\partial v_\perp}{\partial S} - \left(\frac{M^2-1}{\Sigma M^2 v_\perp}\right)\frac{\partial c_s^2}{\partial S}. \tag{11}$$

The sign of $[\omega/\Sigma]$ depends mainly on the gradient of $v_\perp$ (or M) along the shock, and width of vortensity rings correspond to the length along the shock where $|M|$ is increasing with respect to S (if $v_\perp < 0$).

4.2.2. Flow field

In order to estimate the pre-shock flow, we simplify the geometry by adopting the shearing box approximation (e.g. Paardekooper & Papaloizou 2009). We consider a local Cartesian co-ordinate system (x, y) co-rotating with the planet at angular speed Ω_p. The x direction corresponds to radius while y correspond to azimuth. Without the planet, the velocity field is Keplerian $\mathbf{v} = (0, -3\Omega_p x/2)$. The hydrodynamic equations in this frame are

$$\frac{D\Sigma}{Dt} = -\Sigma \nabla \cdot \mathbf{v}, \tag{12}$$

$$\frac{D\mathbf{v}}{Dt} + 2\Omega_p \hat{\mathbf{z}} \wedge \mathbf{v} = -\frac{1}{\Sigma}\nabla P - \nabla \Phi_{\text{eff}}, \tag{13}$$

where D/Dt is the total derivative and

$$\Phi_{\text{eff}} = -\frac{M_p}{\sqrt{x^2 + y^2 + \epsilon^2}} - \frac{3}{2}\Omega_p^2 x^2 \tag{14}$$

is the effective potential with softening length $\epsilon = 0.6 h r_p$.

Next, we assume pressure effects can be ignored compared to planet potential in this local frame. This is appropriate for sufficiently massive planets and/or low pressure; the latter being consistent with shock formation. This enables the velocity field $\mathbf{v}$ to be obtained from Eq. 13 directly. Regarding a fluid particle's motion as $\mathbf{v} = \mathbf{v}(y)$, $x = x(y)$ and writing $\frac{D}{Dt} = v_y\frac{d}{dy}$, its motion can described by

$$\frac{dv_y^2}{dy} = -4\Omega_p v_x - \frac{2M_p y}{(x^2 + y^2 + \epsilon^2)^{3/2}}, \tag{15}$$

$$\frac{d}{dy}\left(v_x v_y^2\right) = v_x \frac{dv_y^2}{dy} + 2\Omega_p v_y^2 + v_y \left[3\Omega_p^2 x - \frac{M_p x}{(x^2 + y^2 + \epsilon^2)^{3/2}}\right], \tag{16}$$

$$\frac{d}{dy}\left(x v_y^2\right) = x\frac{dv_y^2}{dy} + v_x v_y. \tag{17}$$

This particular form imply finite derivatives. We solve for the state vector $\mathbf{v}(y) = [v_y^2, v_x v_y^2, x v_y^2]$ in $x > 0$ for a particular particle. The boundary condition is

$$(v_y, v_x, x) \rightarrow (-3\Omega_p x_0/2, 0, x_0) \text{ as } y \rightarrow \infty, \tag{18}$$

where x_0 is the particle's unperturbed path.

Having obtained the velocity field, we assume vortensity conservation in the pre-shock flow to obtain Σ. From Eq. 8, the surface density is given by

$$\Sigma(x, y) = \frac{2\Sigma_0}{\Omega_p}(\omega_r + 2\Omega_p), \tag{19}$$

where the absolute vorticity at $y = \infty$ is taken as $\Omega_p/2$, ignoring background vorticity variation ($\propto (r_p + x)^{-3/2}$). This is consistent with basic state velocity field in the shearing box. Numerically, the relative vorticity is estimated via circulation:

$$\omega_r \simeq \frac{1}{\Delta A} \oint \mathbf{v} \cdot \mathbf{dl} \qquad (20)$$

where the integration is taken over a closed loop about the point of interest and ΔA is the enclosed area. This avoids numerical differentiation on a non-uniform grid, which is a result of using the Lagrangian approach to obtain $\mathbf{v}$.

4.2.3. Shock front

The physical reason for shock formation is the fact that the planet presents an obstacle to the flow. In subsonic flow, the presence of the obstacle can be communicated to the fluid via sound waves induced by the planet. In supersonic flow, the fluid is unaware of the planet via sound waves (but does feel the planet gravity). The boundary between these two regions, defined by a characteristic curve, is a natural location for shocks. Applying this idea to Keplerian flow, Papaloizou et al. (2004) obtained a good match between this characteristic and wakes associated with a low mass planet. For general velocity field $\mathbf{v}$, this characteristic curve satisfies

$$\frac{dy_s}{dx} = \frac{\hat{v}_y^2 - 1}{\hat{v}_x \hat{v}_y - \sqrt{\hat{v}_x^2 + \hat{v}_y^2 - 1}}, \qquad (21)$$

where $\hat{v}_i = v_i/c_s$. The sign of the square root has been chosen for the domain $x > 0$ ($v_y < 0$). As the fluid flows from super-sonic ($y > y_s$) to sub-sonic ($y < y_s$), fluid on $y = y_s$ is the first to know about the planet through pressure waves (Papaloizou et al. 2004). In Keplerian flow, the ray originates from sonic points $x = \pm 2H/3$, $y = 0$. Interior to this, flow is subsonic and there can be no shock. In general flow, sonic points ($|\mathbf{v}| = c_s$) are curves and can occur for $x < 2hr_p/3$. This means shocks can indeed originate well inside a planet's co-orbital region. There is a locus of possible starting points to solve Eq. 21, for simplicity we take the sonic point with $x = 0$ and the corresponding $y > 0$ that is furthest from the planet.

4.3. Results and discussion

We can now compare hydrodynamic simulations to the model. First we show particle paths and theoretical/simulation shock fronts in Fig. 7. Fluid elements are scattered by the planet and particle paths cross for $x > r_h$, $y < -2r_h$, this means particle dynamics do not give unique velocities here. The solution to Eq. 21 should not be trusted for this region.Fortunately, vortensity generation occurs mostly inside $1 - 1.5r_h$, where paths do not cross and particle dynamics gives a
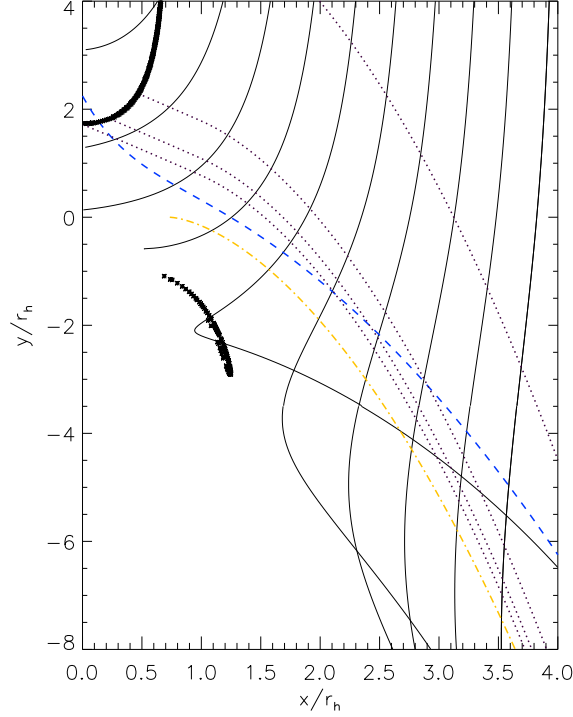
Fig. 7.—: Solid lines: particle paths from the zero-pressure momentum equations (Eq. 12 - 13); thick lines: sonic points $|\mathbf{v}| = c_s$; dotted lines: theoretical shock fronts; dash-dot: solution to Eq. 21 for Keplerian flow; dashed : polynomial fit to simulation shock front. The actual shock front begins around $x = 0.2r_h$, where it crosses the sonic point.

unique velocity along each point on the shock. Also, along the true shock front, paths do not cross.

Fig. 8 shows several combinations of theoretical model and simulation data to giving vortensity jump across the outer spiral shock. The similarity between data and model curves confirm vortensity generation across horse-shoe turns. Assuming fluid is mapped from $x \rightarrow -x$ as it switches to the inner leg of its horse-shoe orbit, we expect the outer spiral shock to produce a vortensity ring peaked at $r - r_p \sim -0.5r_h$ of width $\sim r_h \, (\simeq H)$, and vice versa for the inner shock. Thin vortensity rings are natural features of the co-orbital region for intermediate or massive planets.

Torques from the co-orbital region depends on local disc profile. The relevant profile should be the shock-modified profile because the modification takes place on fast, dynamical time-scales. The double-ring structure should be taken as the 'initial' profile to evaluate co-orbital torques and study migration. Vortensity rings represent variations in disc profile on a length-scale of the local scale-height, which enables dynamical instabilities.
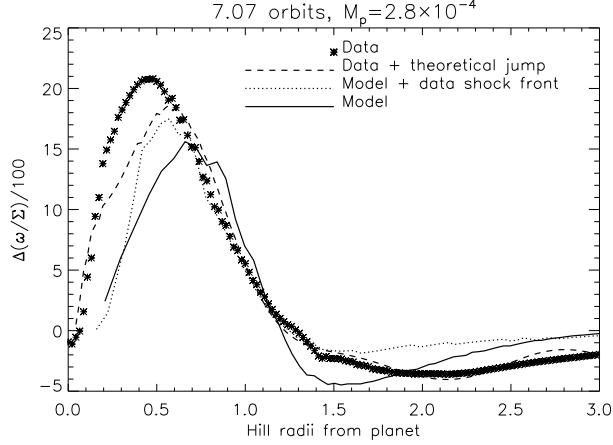
Fig. 8.—: Theoretical and actual vortensity jumps across a shock in the co-orbital region. Asterisks are measured from simulation; the dashed line was obtained by using pre-shock simulation data coupled with the jump condition Eq. 11; dotted line from particle dynamics model with shock front given by simulation; solid curve corresponds to theoretical flow field and shock front.

5. Dynamical stability of vortensity rings

We study the linear stability of the shock-modified protoplanetary disc with double vortensity rings presented above. Linear stability theories of adiabatic perturbations in inviscid tori and discs without a planet are well known for barotropic fluid (Papaloizou & Pringle 1984, 1985; Papaloizou & Lin 1989) and non-barotropic fluid (Lovelace et al. 1999; Li et al. 2000). These studies show steep gradients in disc profile are subject to dynamical instabilities. Our study considers the partial gaps opened by Saturn-mass planets, so results of linear analysis has implications on type III migration, through the effect of the instability on the co-orbital mass deficit.

5.1. Basic state

The governing equation for inviscid, thin gaseous discs are reproduced here for reference:

$$\frac{\partial \Sigma}{\partial t} + \nabla \cdot (\Sigma \mathbf{v}) = 0 \tag{22}$$

$$\frac{\partial \mathbf{v}}{\partial t} + \mathbf{v} \cdot \nabla \mathbf{v} = -\frac{1}{\Sigma} \nabla P - \nabla \Phi \tag{23}$$

with $P = c_s^2 \Sigma$, $c_s^2 = h^2/r$ and $h = $ constant. Φ is the total potential, including the planet which is held on fixed orbit for this linear analysis. Φ is responsible for the vortensity-ring basic state and therefore not perturbed. We study self-excited modes in the disc.

We assume the basic state is axisymmetric, time independent with no radial velocity ($\partial/\partial \phi =$

$\partial/\partial t = v_r = 0$). If the vortensity profile $\eta(r)$ is known (e.g. via shock modelling):

$$\eta(r) = \frac{1}{r\Sigma}\frac{d}{dr}\left(r^2\Omega\right), \tag{24}$$

then combined with the radial momentum equation

$$r\Omega^2 = \frac{1}{\Sigma}\frac{dP}{dr} + \frac{1}{r^2} \tag{25}$$

gives

$$h^2\frac{d^2\ln\Sigma}{dr^2} = \frac{h^2-1}{r^2} - \frac{2h^2}{r}\frac{d\ln\Sigma}{dr} + 2\Sigma\eta\sqrt{\frac{1-h^2}{r} + h^2\frac{d\ln\Sigma}{dr}} \tag{26}$$

as the governing equation for the basic state density. Assuming the rings are pressure-supported against the gravity of the central star, planet and indirect potentials are neglected in Eq. 25. We take $\eta(r)$ from the fiducial simulation in the previous section. Fig. 9 shows η^{-1} for this fiducial case. It is very nearly axisymmetric apart from the region close to the planet. The self-consistent basic state is produced by solving Eq. 26 subject to $\Sigma = 10^{-3}$ (i.e. unperturbed) at $r = 1.1, 3.0$.

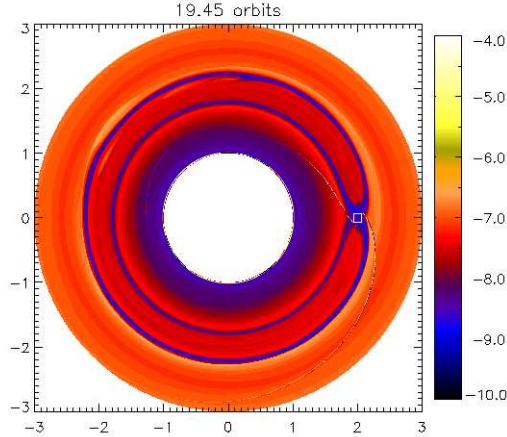There is good agreement between hydrostatic profiles based on vortensity and simulation data

Fig. 9.—: $\ln\Sigma/\omega$ of the basic-state protoplanetary disc under consideration.

in Fig. 10(a)—10(b). Fig. 10(b) show the basic state angular velocity divided by the Keplerian speed. Ω deviates from Keplerian by at most $\sim 1\%$, but it also varies on length-scales $O(H)$. $d\Omega/dr$ is non-Keplerian, and it is the strong shear induced by the shocks that is responsible for instabilities. The validity of Eq. 26 assures us that, even though this is a disc-planet problem, the planet potential is part of the ring-basic state and does not appear in the linearised equations. We may apply standard perturbation theory for discs with protoplanetary disc profiles.
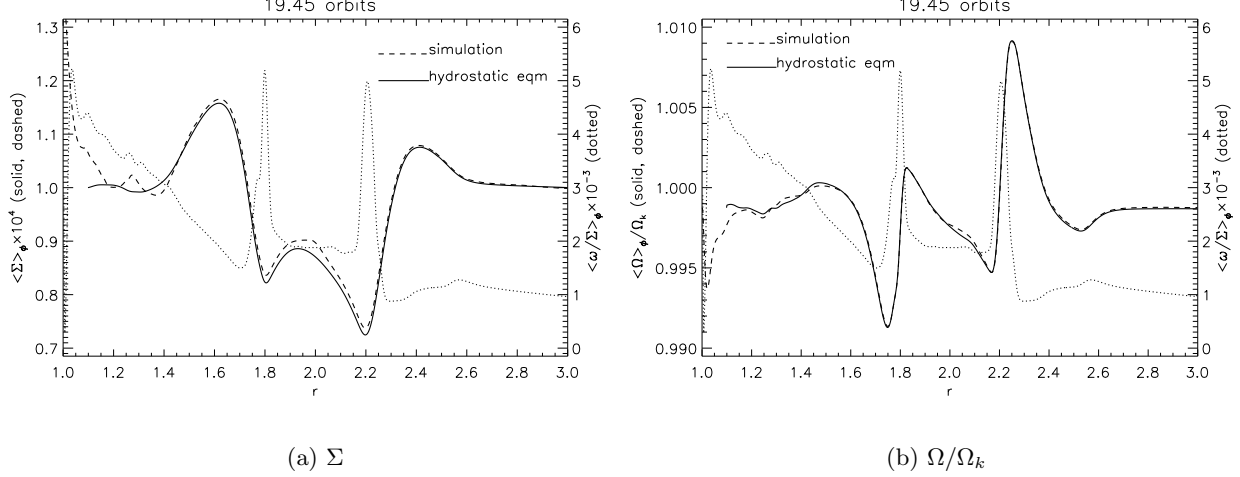
(a) Σ

(b) Ω/Ω_k

Fig. 10.—: Double-ring basic state produced by spiral shocks. The inner boundary for applying hydrostatic equilibrium is taken at $r = 1.1$ instead of $r = 1$ to avoid boundary effects from simulation data.

5.2. Linearised equations

We now derive the governing equation for isothermal perturbations in the protoplanetary disc. We linearise about the basic state

$$(\Sigma, v_r, v_\phi) \to (\Sigma + \delta\Sigma(r), \delta v_r(r), v_\phi + \delta v_\phi(r)) \times \exp i(\sigma t + m\phi) \tag{27}$$

where σ is a complex frequency and m is the azimuthal wavenumber. m is required to be an integer for physical solutions (which without loss of generality can be taken positive). The pressure perturbation is $\delta P = c_s^2 \delta\Sigma$. Using the fractional density perturbation $W \equiv \delta\Sigma/\Sigma$ as the key variable, the linearised continuity equation (Eq. 22) is

$$i\bar{\sigma}W = -\frac{1}{r\Sigma}\frac{d}{dr}\left(r\Sigma\delta v_r\right) - \frac{im}{r}\delta v_\phi \tag{28}$$

and the linearised momentum equations (Eq. 23) are

$$\delta v_r = -\frac{h^2}{r(\kappa^2 - \bar{\sigma}^2)}\left(i\bar{\sigma}\frac{dW}{dr} + \frac{2im\Omega W}{r}\right) \tag{29}$$

$$\delta v_\phi = \frac{h^2}{r(\kappa^2 - \bar{\sigma}^2)}\left(\Sigma\eta\frac{dW}{dr} + \frac{m\bar{\sigma}}{r}W\right), \tag{30}$$

where

$$\kappa^2 = 2\Omega\Sigma\eta \tag{31}$$

is the epicycle frequency in terms of vortensity η and

$$\bar{\sigma} \equiv \sigma + m\Omega(r) = \underbrace{\sigma_R + m\Omega(r)}_{\bar{\sigma}_R} + i\gamma$$

is the Doppler-shifted frequency (σ_R, γ real). The linearised equations can be combined to give the governing equation

$$\frac{d}{dr}\left(\frac{\Sigma}{\kappa^2 - \bar{\sigma}^2}\frac{dW}{dr}\right) + \left\{\frac{m}{\bar{\sigma}}\frac{d}{dr}\left[\frac{\kappa^2}{r\eta(\kappa^2 - \bar{\sigma}^2)}\right] - \frac{r\Sigma}{h^2} - \frac{m^2\Sigma}{r^2(\kappa^2 - \bar{\sigma}^2)}\right\}W = 0. \tag{32}$$

This is an eigenvalue problem with complex eigenvalue σ hidden in $\bar{\sigma}$.

5.3. Necessary condition for instability

It is useful to simplify Eq. 32 to gain further insight. To to this we consider special modes, the co-rotational modes were $\kappa^2 \gg |\bar{\sigma}^2|$. Now, recognising $h^2/r = c_s^2$, the ratio of the last two terms in Eq. 32 is

$$\frac{r^2\kappa^2}{m^2 c_s^2} \sim \frac{1}{m^2}\frac{v_\phi^2}{c_s^2} \sim \frac{1}{m^2 h^2}.$$

For a thin disc $h \ll 1$, so if $m = O(1)$ this ratio is large and the last term in Eq. 32 can be neglected. In this limit Eq. 32 reduces to

$$\frac{d}{dr}\left(\frac{rc_s^2\Sigma}{\kappa^2}\frac{dW}{dr}\right) + \left\{\frac{m}{\bar{\sigma}}\frac{d}{dr}\left[\frac{c_s^2}{\eta}\right] - r\Sigma\right\}W = 0, \tag{33}$$

we have re-inserted the sound speed so that Eq. 33 applies to any fixed temperature profile. The $-r\Sigma W$ term suggests exponential decay as $r \to 0, \infty$. The vortensity term is required to joined smoothly the exponential from either side. We expect such modes to be localised around co-rotation, $\bar{\sigma} = 0$. The locality is verified by numerical solutions.

Multiplying Eq. 33 by W^* and integrating between $[r_1, r_2]$ assuming $W = 0$ or $dW/dr = 0$ at boundaries we have:

$$\int_{r_1}^{r_2}\frac{m}{\bar{\sigma}}\left(\frac{c_s^2}{\eta}\right)'|W|^2 dr = \int_{r_1}^{r_2} r\Sigma|W|^2 dr + \int_{r_1}^{r_2}\frac{r\Sigma c_s^2}{\kappa^2}|W'|^2 dr \tag{34}$$

where $' \equiv d/dr$. Since the RHS is real, the imaginary part of LHS must vanish:

$$-i\gamma\int_{r_1}^{r_2}\frac{m}{(\sigma_R + m\Omega)^2 + \gamma^2}\left(\frac{c_s^2}{\eta}\right)'|W|^2 dr = 0, \tag{35}$$

so non-neutral modes ($\gamma \neq 0$) require $(c_s^2/\eta)' = 0$ at some r in $[r_1, r_2]$. The standard profile $c_s^2 \propto 1/r$ imply temperature variations on $L \sim O(r)$, but η varies on $H \ll r$. Effectively, the vortensity profile $\eta(r)$ needs to contain stationary points for unstable modes. This point should coincide with co-rotation r_0 to ensure regularity at $\bar{\sigma} = 0$. Papaloizou & Lin (1989) has shown that vortensity maxima are stable while minima are unstable. Although their analysis consider barotropic discs, conclusions apply here. provided that co-rotational modes are localised so $c_s^2 \sim$ const. in the region of interest, equivalently a barotropic equation of state locally.

From Fig. 10(a), it is clear that the shock-modified protoplanetary disc satisfies the necessary criterion for instability. Standard power-law Keplerian discs ($\Omega = r^{-3/2}$, $\Sigma \propto r^{-p}$, $p > 0$) do not contain local vortensity maximum or minimum and do not support this instability.

5.4. Limit on the growth rate

We show the growth rate is physically limited by local shear. This is a self-consistency check because the equation for co-rotational modes (Eq. 33) assumes $\kappa^2 \ll |\bar{\sigma}^2|$. Since $\kappa \sim \Omega$, this simplification implies the growth rate $|\gamma|/\Omega \ll 1$. Nevertheless, it is useful to obtain a quantitative estimate of an upper limit to the growth rate, which provide bounds on initial guess values when solving the eigenvalue problem numerically. Let

$$W = g\bar{\sigma}, \tag{36}$$

Eq. 33 then gives the alternative form:

$$\left(\frac{r\Sigma c_s^2 \bar{\sigma}^2}{\kappa^2} g' \right)' = \bar{\sigma} \left[r\Sigma\bar{\sigma} - m \left(\frac{c_s^2}{\eta} + \frac{r\Sigma c_s^2 \Omega'}{\kappa^2} \right)' \right] g \tag{37}$$

$$= \bar{\sigma} \left[r\Sigma\bar{\sigma} - m \left(\frac{c_s^2 \Sigma}{2\Omega} \right)' \right] g,$$

where we used $\bar{\sigma}' = m\Omega'$ and on the second line used Eq. 24 and Eq. 31. The vortensity is now implicit in Σ and Ω. Multiplying Eq. 37 by g^*, integrating and neglecting boundary terms gives

$$- \int_{r_1}^{r_2} \frac{r\Sigma c_s^2 \bar{\sigma}^2}{\kappa^2} |g'|^2 dr = \int_{r_1}^{r_2} \bar{\sigma} \left[r\Sigma\bar{\sigma} - m \left(\frac{c_s^2 \Sigma}{2\Omega} \right)' \right] |g|^2 dr. \tag{38}$$

The real part is

$$\gamma^2 \int_{r_1}^{r_2} r\Sigma \left(\frac{c_s^2}{\kappa^2} |g'|^2 + |g|^2 \right) dr = \int_{r_1}^{r_2} \left[r\Sigma\bar{\sigma}_R^2 \left(\frac{c_s^2}{\kappa^2} |g'|^2 + |g|^2 \right) - m\bar{\sigma}_R \left(\frac{c_s^2 \Sigma}{2\Omega} \right)' |g|^2 \right] dr, \tag{39}$$

and the imaginary part is (assuming $\gamma \neq 0$):

$$\int_{r_1}^{r_2} \left[2r\Sigma\bar{\sigma}_R \left(\frac{c_s^2}{\kappa^2} |g'|^2 + |g|^2 \right) - m \left(\frac{c_s^2 \Sigma}{2\Omega} \right)' |g|^2 \right] dr = 0. \tag{40}$$

Eq. 39 and Eq. 40 can be combined to give:

$$\int_{r_1}^{r_2} r\Sigma(\gamma^2 + \sigma_R^2) \left(\frac{c_s^2}{\kappa^2} |g'|^2 + |g|^2 \right) dr = \int_{r_1}^{r_2} m^2\Omega^2 r\Sigma \left(\frac{c_s^2}{\kappa^2} |g'|^2 + |g|^2 \right) dr \tag{41}$$

$$- \int_{r_1}^{r_2} m^2\Omega \left(\frac{c_s^2 \Sigma}{2\Omega} \right)' |g|^2 dr.$$

Comparing coefficients of $|g|^2$ in the integrand on RHS (for the case $h = 0.05$, basic state from simulations):

$$\left| \frac{m^2 \Omega^2 r \Sigma}{m^2 \Omega \left(\frac{c^2 \Sigma}{2\Omega} \right)'} \right| \gtrsim 92. \tag{42}$$

So the last term on RHS of Eq. 41 can be neglected [1] .

Next, consider the inequality

$$0 \geqslant m^2 \int_{r_1}^{r_2} (\Omega - \Omega_+)(\Omega - \Omega_-) r \Sigma \left(\frac{c^2}{\kappa^2} |g'|^2 + |g|^2 \right) dr \tag{43}$$

where Ω_+, Ω_- are the maximum and minimum angular speed in the range of integration. Using approximation Eq. 42 in Eq. 40, combined with the inequality, one can show

$$\gamma^2 + \left[\sigma_R + \frac{1}{2} m(\Omega_+ + \Omega_-) \right]^2 \leqslant m^2 \left(\frac{\Omega_+ - \Omega_-}{2} \right)^2. \tag{44}$$

The complex eigenfrequency σ is contained inside a circle centred on the real axis at $m(\Omega_+ + \Omega_-)/2$ with radius $m(\Omega_+ - \Omega_-)/2$. Furthermore, if the mode is localised about r_0 with characteristic width $\Delta > 0$ and the angular speed is monotonically decreasing then

$$\Omega_\pm \simeq \Omega(r_0) \mp \Omega'(r_0)\Delta$$

so that

$$\gamma^2 + [\sigma_R + m\Omega(r_0)]^2 \leqslant \left(m\Omega'(r_0)\Delta \right)^2, \tag{45}$$

which show growth rates γ of co-rotational modes are limited by the local shear. The upper limit to $|\gamma|$ can be increased if $\sigma_R + m\Omega(r_0) = 0$. The instability operates on dynamical time-scales which will affect planet migration, which occur on longer time-scales. This validates linear analysis assuming the planet has fixed orbit. In reality the planet would not migrate significantly before the instability grows, especially if the migration is induced by the instability.

5.5.   Numerical solutions

We use the standard shooting method with adaptive Runge-Kutta integrator and multi-dimensional Newton root-finding (Press et al. 1992) to solve the full equation Eq. 32. The basic state $\Sigma(r)$ and $v_\phi(r)$ was calculated numerically by imposing hydrostatic equilibrium given the simulation vortensity profiles. We search for unstable modes ($\gamma < 0$) with $\sigma_R \simeq -m\Omega(r_0)$. In the discs considered, $r_0 = 1.7$, 2.3 are the inner, outer vortensity minima respectively. r_0 defines the gap edges.

---

[1]To order of magnitude, if the length scale of variation $L \sim O(r)$ then this ratio is $O(h^{-2})$; if $L \sim O(H)$ then the ratio is $O(h^{-1})$. In either case the ratio is $\gg 1$.

5.5.1. Example: $m = 3$

The modulus of eigenmodes for $m = 3, h = 0.05$ are shown relative to background vortensity in Fig. 11 for inner/outer edges. For simplicity we set $W = 0$ at the boundary. The instability is associated with vortensity minima, which was observed by Li et al. (2005) in simulations. For Saturn, vortensity rings lie near the separatrix, approximately separating regions where shocks generate/destroy vortensity. Solutions are evanescent near co-rotation, decaying away from r_0. Vortensity peaks (which coincide with peaks in epicycle frequency κ^2) behave like walls to damp the instability. Lindblad resonances (when $\kappa^2 - \bar{\sigma}^2 = 0$) occur at $r_L/r_0 = 0.76, 1.21$ where waves are emitted. Waves can be identified towards the inner (outer) boundary for the outer (inner) edges, even with a zero boundary condition. However, waves are not obvious towards the inner (outer) boundary for modes focused on inner (outer) edges. This is because the inner (outer) boundaries are not sufficiently far away from inner (outer) edges. We find that changing boundary conditions does not alter the qualitative behaviour in Fig. 11.

The oscillatory amplitude is at most $\simeq 20\%$ of that at r_0, and even less for $m < 3$. The dominant effect of low m modes will be due to perturbations near co-rotation. The evanescent wave grows in time at edges whereas the planet reside inside the gap. Therefore such modes are most relevant for type III migration — interaction between circulating fluid and the co-orbital region. Typical disc-planet simulation setups give an inwards migration initially, thus the planet interacts with the inner edge mode. The growth time-scale of the inner mode, in terms of the orbital period at $r = 2$ is $\sim 14P$. After this we expect non-linear evolution, and it has been observed that vortices merge into a single vortex (Koller et al. 2003; de Val-Borro et al. 2007). In the fiducial simulation of migrating planet, rapid migration begins at $55P$ which is compatible with the time-scale be become non-linear.

Fig. 11 shows the outer edge is more unstable than inner edge. We checked with simulations which show vortex-development at the outer edge first. Fig. 11 show vortensity peaks of similar height, but the inner η-minima is larger than outer because the background vortensity $\propto r^{-3/2}$. In this case the outer edge is more extreme (steeper gradients) and therefore becomes unstable first.

5.6. Growth rates as a function of m and h

Co-rotational modes are most relevant to co-orbital disc-planet interactions. For completeness we briefly discuss stability as a function of wave number m and h. We abbreviate $h = 0.05$ as h_5...etc.. Waves stabilise the mode by carrying energy away from co-rotation, consequently $|\gamma|$ eventually decrease as m increases. Waves from either side of co-rotation is joined by the vortensity term (Eq. 32) near r_0. However, increasing m weakens this term, so for sufficiently large m a mode cannot be constructed. A cut-off of $|\gamma|$ as a function of m is expected, allowing us to distinguish between physical and unphysical modes, and to extrapolate results where needed.
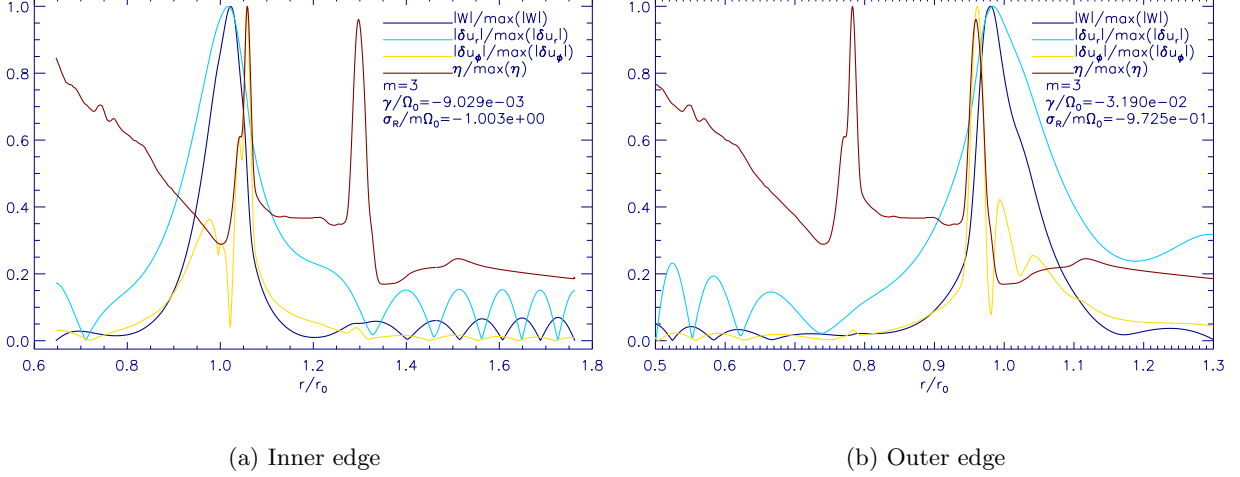
(a) Inner edge

(b) Outer edge

Fig. 11.—: $m = 3$ eigenmodes with zero boundary condition. η is the background vortensity profile.

We solved Eq. 32 subject to WKB radiative boundary condition and non-integer m to map out dependence of γ on azimuthal wave number. If the cut-off value is small then only considering integer m is not sufficient to determine a quantitative relation. There is no mathematical requirement that $m \in \mathbb{Z}$ but only integer values are physically realisable. Results are shown in Fig. 12 with polynomial fits and extrapolation.
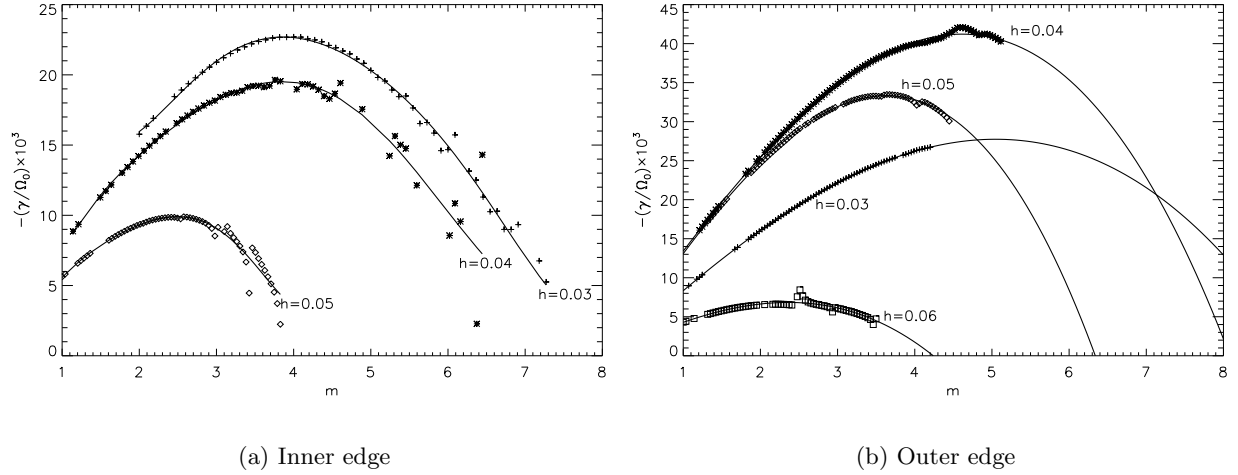

(a) Inner edge

(b) Outer edge

Fig. 12.—: Growth rates as a function of azimuthal wave number m and aspect ratio h. Ω_0 is background angular speed at corresponding vortensity minima. The $h = 0.03$ case for the outer edge is spurious because the vortensity profile is not representative of the disc structure.

Inner edge growth rates in the standard disc h_5 peaks at $m = 2$—3 and extrapolation suggest

a cut-off for $m \geq 5$. Decreasing to h_4, $|\gamma|$ peaks around $m = 4$ with growth rate roughly twice the peak of h_5. Higher-m modes are enabled as temperature is lowered; and de Val-Borro et al. (2007) found growth rates for the gap associated with Jupiter-mass planet to peak at $m = 4$—6. Both decreasing h and increasing planet mass produce steeper radial gradients in disc profile, making it less stable.

A similar behaviour was found for the outer edge, with the exception of h_3 being spurious . We were unable to find self-consistent modes ($|\gamma|$ monotonic with respect to m) beyond the peaks for h_4, h_5 because the outer boundary is not sufficiently far from co-rotation [2]. In this case we extrapolate to higher m with polynomials, assuming there is some cut-off at high m. For the outer edge, generally being less stable, modes were found for $h = 0.06$, but not for inner edge.

The rates are an order of magnitude smaller than those obtained by de Val-Borro et al. (2007) for Jupiter-mass planet gaps. However, the instability still operates on a time-scale that affect migration, particularly via type III for our Saturn-mass planet due to partial gaps.

6. Vortex-induced type III migration

Having understood where vortices originate from through linear stability analysis, we are ready to apply some of the results above to disc-planet interactions. We shall consider the effect of changing disc temperature, or equivalently the aspect ratio h, and the surface density on type III migration in an inviscid disc. The resolution was $N_r \times N_\phi = 512 \times 1536$ and the planet potential switched on over 5 orbital periods. The connection to type III migration lies in the co-orbital mass deficit: $\delta m = 4\pi x_s r_p (\Sigma_v - \Sigma_g)$. Σ_g is the gap density and Σ_v the density at the inner edge . Co-rotational modes are the relevant perturbations because they are localised near the gap edge thereby increasing Σ_v (and further enhanced by vortex formation) but not Σ_g. Hence δm grows due to instability, which promotes type III migration.

6.1. Variable h

An implication linear analysis is dependence of γ on aspect ratio h. Let us consider vortex-effects when $h = 0.04$—0.06 and fixed initial surface density $\Sigma = 7 \times 10^{-4}$. The migration evolution with h_3 is somewhat different because the instability develops during ring-formation, unlike higher h where rings form first, then the instability sets in. We omit h_3 for comparison purposes. Fig. 13 shows Σ/ω near the planet as a function of h and agree with linear theory, showing that disturbances are focused at gap edges.

---

[2]Similar effect at inner edges as growth rates become more sporadic after the peaks, although these modes satisfy the correct physical picture of being wave-like towards boundaries and evanescent near co-rotation.

Both edges become more unstable for lower h. h_6 remains relatively stable, although some vortices are identified inside the co-orbital region. We identify an $m = 4$ mode on h_4 inner edge which has peak growth rate from theory (Fig. 12). A weak $m = 2$ mode is observed for h_5, which coincides with peak rates ($m = 2$–3 for h_5). Disturbances at outer edges have higher growth rates, and have already undergone merging into large vortices. As the planet is migrating inwards, we expect interaction with inner edge vortices to occur sooner for lower h.

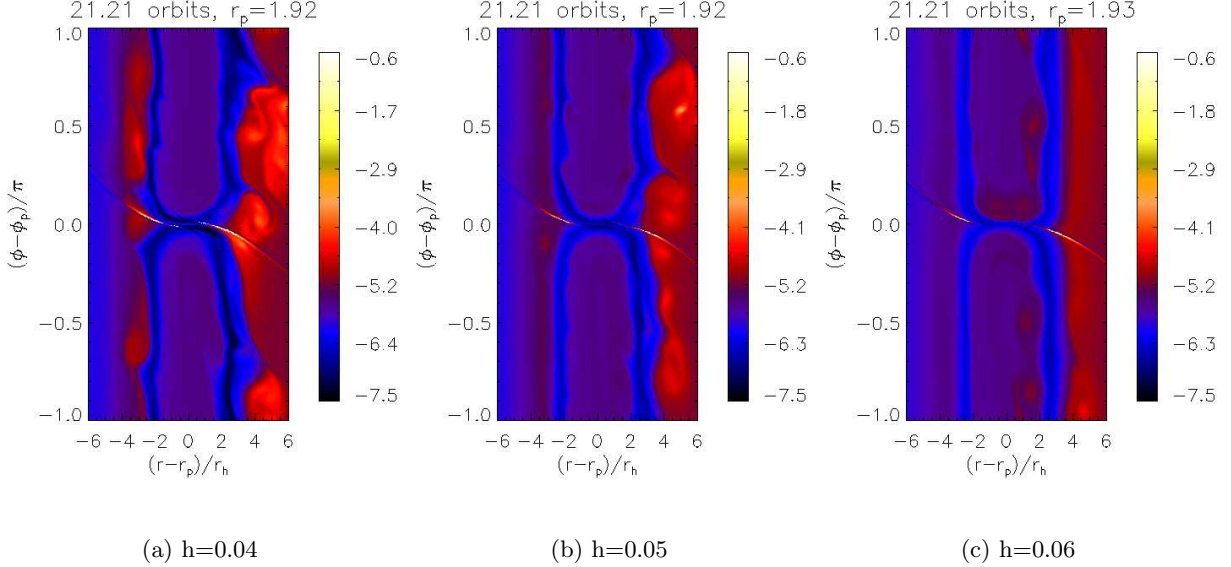(a) h=0.04   (b) h=0.05   (c) h=0.06

Fig. 13.—: Inverse vortensity Σ/ω near co-orbital region (logarithmic scale), as a function temperature.

Fig. 14 show corresponding migration curves. Although linear analysis assumes the planet had fixed orbit, and therefore strictly not applicable in the migrating case; we have seen previously that vortensity rings acts inhibit type III migration as long as they are not disrupted. In Fig. 14 the stronger vortensity rings associated with h_4 results in almost no migration during slow phases. During these stages the planet is has effectively fixed orbit, so results of linear theory can be applied. In h_4, rapid migration begins at $t = 25$, roughly half the time needed than h_5. The extent of orbital decay during rapid migration is unchanged (few r_h), consistent with the notion that the vortex development implies a co-orbital mass deficit, for which a critical value reached enables rapid migration and determines migration extent.

More episodes of rapid migration occur in h_4 because growth rates are larger. The slow phase is also non-smooth compared to h_5 due oscillatory torques exerted by vortices. This is not apparent in the migration curve of h_5 because perturbations have smaller amplitudes at a given time. Notice in h_4 the waiting time increases and the extent of migration decreases. As the planet migrate inwards, its co-orbital width decreases ($x_s \propto r_p$), the vortex flows across a smaller region during its encounter with the planet, implying smaller change in vortex specific angular momentum. If the
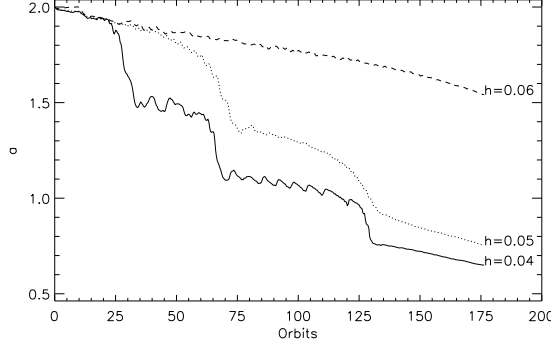
Fig. 14.—: Vortex-induced migration in inviscid discs with different aspect ratio h but same initial uniform density $\Sigma = 7 \times 10^{-4}$.

vortex mass is the same or smaller in later episodes, then there is decreasing angular momentum loss by the planet, which explains smaller orbital decay in subsequent episodes.

In h_6 no rapid migration was observed within simulation time. This is consistent with linear theory where co-rotational nodes for the inner edge were not found, and with Fig. 13 where the inner edge remains unperturbed. There is no vortex that grows sufficient size to induce rapid migration. This suggest that disc temperature must be sufficiently low for vortex-planet interactions to occur.

6.2. Variable disc mass

Here, we consider discs with initially uniform density of $\Sigma_0 \times 10^{-4}$ and aspect ratio $h = 0.05$. Fig. 15 show migration curves from these simulations. For $\Sigma_0 = 5$—9, the decrease in semi-major axis a is the same for the first rapid migration and the planet stalls at the same radius. This is observed for a second episode for $\Sigma_0 = 6$—9. These results imply that during the vortex-planet interaction, the planet loses approximately the same amount of angular momentum independent of Σ_0. The same amount of angular momentum is transferred to disc material, the vortex. The vortex flows across the co-orbital region, of size determined by planet mass which has been fixed. This means the change in specific angular momentum of the vortex is the same , which implies the same mass of vortex, M_v, interacts with the planet for difference Σ_0. Rapid migration is initiated by sufficient contrast between co-orbital (gap) and circulating fluid (vortex) measured by, say δm, which also determines migration extent. Vortices originate from instabilities with growth rates independent of Σ_0, so increasing Σ_0 means less time is needed for the vortex to reach critical density or mass. Hence, the 'waiting time' before rapid migration is shortened with increasing surface density. On the other hand, if the surface density is too low, e.g. $\Sigma_0 = 3$ then vortex-induced rapid migration can not occur.

The vortex mass is limited by the amount of material that can be gathered at formation radius

(the gap edge):

$$M_v < 2\pi \alpha r_h r_v \Sigma;$$

where r_v is the vortex orbital radius and αr_h represents its width. From simulation, the fiducial case ($\Sigma_0 = 7$), $M_v/M_p \sim 3.5$, which gives

$$\Sigma_0 > \frac{3.5 M_p}{2\pi \alpha f_0 (1 - \beta f_0) r_p^2} \times 10^4 \qquad (46)$$

as the lower limit for surface density. f_0 is such that $r_h = f_0 r_p$ and $r_v = (1 - \beta f_0) r_p$. α, β are simply constants in this simple description. From simulations, inserting $\alpha = 3$, $\beta = 4$ and $r_p \sim 2$ gives $\Sigma_0 \gtrsim 3.5$, for which vortex-induced migration was observed (Fig.15) but not for $\Sigma_0 = 3$. This is similar to the usual requirement that type III migration, occur with intermediate planets in sufficiently massive discs (Masset & Papaloizou 2003), except in our case the limitation is specifically on vortex mass.

6.2.1. Critical co-orbital mass deficit

We measured the co-orbital mass deficit δm for the above cases. This amounts to comparing the average density between co-orbital fluid and circulating fluid just behind the planet (see Eq. 3). Results are show in Fig. 16. $\Sigma_0 = 3$ is qualitatively different, it does not show rapid migration and typically $\delta m \lesssim 3$ with smaller amplitudes. Cases with rapid migration evolve similarly.

δm is initially zero since the background density is flat, and first increases as the planet opens a partial gap. It subsequently also increases due to instability of the gap edge and oscillations signify development of non-axisymmetric density structures that circulate the gap edge. As δm reach $\delta m \sim 4$–5 vortex-planet interaction occurs and migration begins to accelerate (Fig. 15). During the interaction, vortex material within the gap makes δm highly time-dependent. As the vortex
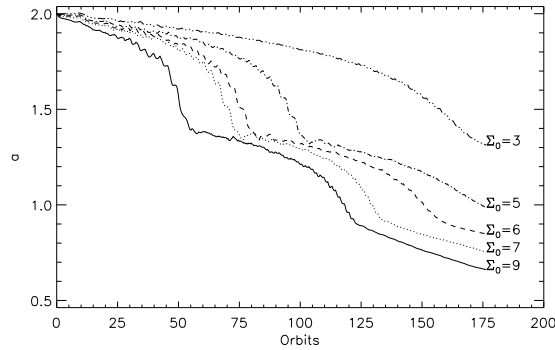

Fig. 15.—: Vortex-induced migration in discs with variable initial densities. The extent of rapid migration is independent of initial surface density.

flows across and increases gap density, δm decreases, eventually $\delta m < 0$ and migration stalls. The vortex is responsible for both rapid migration and stalling, depending whether or not it is in the circulating or co-orbital region.

(a) $\Sigma_0 = 7$ (b) $\Sigma_0 = 5$ (c) $\Sigma_0 = 3$
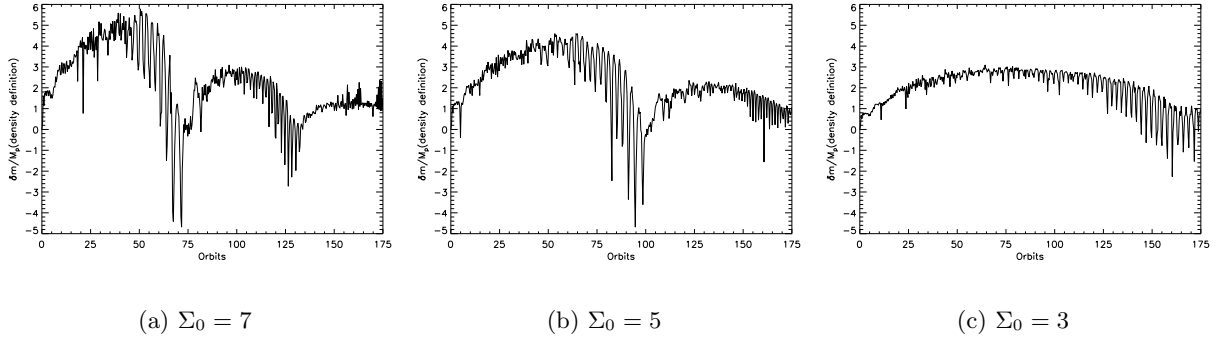
Fig. 16.—: Evolution of the co-orbital mass deficit.

7. Conclusions

We have studied type III migration of Saturn-mass planets in low viscosity discs. Numerical simulations and semi-analytical modelling show that thin vortensity rings are generated through spiral shocks that extend close to planet's orbital radius, as fluid elements make a horse-shoe turn. The double-vortensity rings are hydrostatic and linear stability analysis show the associated vortensity minima are unstable. Growth of co-rotational modes with disturbances localised at the minima increases the density/vortensity contrast between librating and circulating fluid near the co-orbital region, and hence favours type III migration by increasing δm. Linear theory correctly predicts that lowering disc temperature enhances the instability by increasing shock strength so rapid migration occurs earlier. Rapid migration is induced when a vortex, which develops from the non-linear evolution of the instability, flows across the co-orbital region. We have also applied the concept of co-orbital mass deficit in analysing migration.

REFERENCES

Artymowicz, P. 2004a, in Astronomical Society of the Pacific Conference Series, Vol. 324, Debris Disks and the Formation of Planets, ed. L. Caroff, L. J. Moon, D. Backman, & E. Praton, 39–+

Artymowicz, P. 2004b, in KITP Conference: Planet Formation: Terrestrial and Extra Solar

de Val-Borro, M., Artymowicz, P., D'Angelo, G., & Peplinski, A. 2007, A&A, 471, 1043

de Val-Borro, M. e. 2006, MNRAS, 370, 529

Goldreich, P., & Tremaine, S. 1979, ApJ, 233, 857

—. 1980, ApJ, 241, 425

Kevlahan, N.-R. 1997, J. Fluid Mech., 341, 371

Koller, J., Li, H., & Lin, D. N. C. 2003, ApJ, 596, L91

Li, H., Colgate, S. A., Wendroff, B., & Liska, R. 2001, ApJ, 551, 874

Li, H., Finn, J. M., Lovelace, R. V. E., & Colgate, S. A. 2000, ApJ, 533, 1023

Li, H., Li, S., Koller, J., Wendroff, B. B., Liska, R., Orban, C. M., Liang, E. P. T., & Lin, D. N. C. 2005, ApJ, 624, 1003

Lin, D. N. C., & Papaloizou, J. 1986, ApJ, 309, 846

Lovelace, R. V. E., Li, H., Colgate, S. A., & Nelson, A. F. 1999, ApJ, 513, 805

Masset, F. 2000a, A & AS, 141, 165

Masset, F. S. 2000b, in Astronomical Society of the Pacific Conference Series, Vol. 219, Disks, Planetesimals, and Planets, ed. G. Garzón, C. Eiroa, D. de Winter, & T. J. Mahoney, 75–+

Masset, F. S. 2002, A&A, 387, 605

Masset, F. S., & Papaloizou, J. C. B. 2003, ApJ, 588, 494

Mayor, M., & Queloz, D. 1995, Nature, 378, 355

Ou, S., Ji, J., Liu, L., & Peng, X. 2007, ApJ, 667, 1220

Paardekooper, S.-J., & Papaloizou, J. C. B. 2009, MNRAS, 394, 2297

Papaloizou, J. C. B. 2005, Celestial Mechanics and Dynamical Astronomy, 91, 33

Papaloizou, J. C. B., & Lin, D. N. C. 1989, ApJ, 344, 645

Papaloizou, J. C. B., Nelson, R. P., Kley, W., Masset, F. S., & Artymowicz, P. 2007a, in Protostars and Planets V, ed. B. Reipurth, D. Jewitt, & K. Keil, 655–668

Papaloizou, J. C. B., Nelson, R. P., Kley, W., Masset, F. S., & Artymowicz, P. 2007b, Protostars and Planets V, 655

Papaloizou, J. C. B., Nelson, R. P., & Snellgrove, M. D. 2004, MNRAS, 350, 829

Papaloizou, J. C. B., & Pringle, J. E. 1984, MNRAS, 208, 721

—. 1985, MNRAS, 213, 799

Pepliński, A., Artymowicz, P., & Mellema, G. 2008a, MNRAS, 386, 164

—. 2008b, MNRAS, 386, 179

—. 2008c, MNRAS, 387, 1063

Press, W. H., Teukolsky, S. A., Vetterling, W. T., & Flannery, B. P. 1992, Numerical recipes in FORTRAN. The art of scientific computing, ed. W. H. Press, S. A. Teukolsky, W. T. Vetterling, & B. P. Flannery

Stone, J. M., & Norman, M. L. 1992, ApJS, 80, 753

Ward, W. R. 1997, Icarus, 126, 261

A. Upper limit on the horse-shoe width

We deduce an upper limit on the horse-shoe width (x_s) in the limit of zero-pressure, i.e. particle dynamics. Consider a local Cartesian frame centred about the planet and consider a particle approaching the planet from $x = x_0 > 0$, $y = \infty$ with velocity $(0, -3\Omega_p x_0/2)$ where Ω_p is the planet angular speed, which we take as Keplerian $(= r_p^{-3/2})$. Suppose this particle executes a horse-shoe turn and crosses the planet orbit at $q = (0, y)$ with velocity $(v_x, 0)$. We wish to determine the maximum allowed value of x_0.

The particle dynamics equations

$$\frac{D\mathbf{v}}{Dt} + 2\Omega_p \hat{\mathbf{z}} \wedge \mathbf{v} = -\nabla \Phi_{\text{eff}}, \tag{A1}$$

$$\Phi_{\text{eff}} = -\frac{M_p}{\sqrt{x^2 + y^2}} - \frac{3}{2}\Omega_p^2 x^2, \tag{A2}$$

imply the conservation of

$$J = \frac{1}{2}\mathbf{v}^2 + \Phi_{\text{eff}} \tag{A3}$$

along the particle path. Equating J at $(x, y) = (x_0, \infty)$ and q give

$$-\frac{3}{8}\Omega_p^2 x_0^2 = \frac{1}{2}v_x^2 - \frac{M_p}{y}. \tag{A4}$$

The steady-state equation of motion for v_y evaluated at q is

$$v_x \partial_x v_y + 2\Omega_p v_x = -M_p/y, \tag{A5}$$

since $v_x < 0$, $\partial_x v_y < 0$ we deduce

$$|v_x| > \frac{M_p}{2\Omega_p y^2}. \tag{A6}$$

Combining Eq. A4 and Eq. A6:

$$-\frac{3}{8}\Omega_p^2 x_0^2 > \frac{M_p^2}{8\Omega_p^2 y^4} - \frac{M_p}{y}. \tag{A7}$$

Writing $x_0 = \hat{x}_0 r_h$, $r_h = (M_p/3)^{1/3} r_p$ and equivalently for y, we have

$$\hat{x}_0 < \sqrt{\frac{8}{\hat{y}} - \frac{3}{\hat{y}^4}} \lesssim 2.3. \tag{A8}$$

We deduce particles executing a U-turn could not have originated further than 2.3 Hill radii away.

B. Vorticity jump across an isothermal shock

Consider a shock rotating with planet angular velocity $\Omega_p \hat{\mathbf{z}}$. Let (x_1, x_2) be co-ordinates along and normal to the shock and (h_1, h_2) be corresponding scale factors respectively. The $\hat{\mathbf{z}}$-component of relative vorticity ω_r is

$$\omega_r = \frac{1}{h_1}\frac{\partial u_2}{\partial x_1} + \frac{u_2}{h_1 h_2}\frac{\partial h_2}{\partial x_1} - \frac{u_1}{h_1 h_2}\frac{\partial h_1}{\partial x_2} - \frac{1}{h_2}\frac{\partial u_1}{\partial x_2}. \tag{B1}$$

Assuming a steady shock, the x_1 equation of motion is

$$\frac{u_1}{h_1}\frac{\partial u_1}{\partial x_1} + \frac{u_1 u_2}{h_1 h_2}\frac{\partial h_1}{\partial x_2} + \frac{u_2}{h_2}\frac{\partial u_1}{\partial x_2} - \frac{u_2^2}{h_1 h_2}\frac{\partial h_2}{\partial x_1} = -\frac{1}{\rho h_1}\frac{\partial P}{\partial x_1} - \frac{1}{h_1}\frac{\partial \Phi}{\partial x_1} + 2\Omega_p u_2,$$

from which the last term on RHS of Eq. B1 can be replaced:

$$-\frac{1}{h_2}\frac{\partial u_1}{\partial x_2} = -\frac{u_2}{h_1 h_2}\frac{\partial h_2}{\partial x_1} + \frac{u_1}{u_2 h_1}\frac{\partial u_1}{\partial x_1} + \frac{u_1}{h_1 h_2}\frac{\partial h_1}{\partial x_2} + \frac{1}{\rho u_2 h_1}\frac{\partial P}{\partial x_1} + \frac{1}{u_2 h_1}\frac{\partial \Phi}{\partial x_1} - 2\Omega_p, \tag{B2}$$

where P is the pressure and Φ the total potential (which is continuous). The relative vorticity is then

$$\omega_r = \frac{1}{h_1}\frac{\partial u_2}{\partial x_1} + \frac{u_1}{u_2 h_1}\frac{\partial u_1}{\partial x_1} + \frac{1}{\rho u_2 h_1}\frac{\partial P}{\partial x_1} + \frac{1}{u_2 h_1}\frac{\partial \Phi}{\partial x_1} - 2\Omega_p. \tag{B3}$$

The jump in relative vorticity is

$$[\omega_r] = \left(\frac{1}{h_1}\frac{\partial u_2}{\partial x_1}\right)_{\text{post}} + \left(\frac{u_2}{h_1 h_2}\frac{\partial h_2}{\partial x_1}\right)_{\text{post}} - \left(\frac{u_1}{h_1 h_2}\frac{\partial h_1}{\partial x_2}\right)_{\text{post}} - \left(\frac{1}{h_2}\frac{\partial u_1}{\partial x_2}\right)_{\text{post}} - \omega_r.$$

Here subscript 'post' denote post-shock and no subscripts denote pre-shock. For an isothermal shock,

$$\frac{u_2}{(u_2)_{\text{post}}} = M^2 = \frac{(\rho)_{\text{post}}}{\rho},$$ (B4)

where $M = u_2/c_s$ is the pre-shock perpendicular Mach number. Using Eq. B2 to replace the middle three terms on RHS of Eq. B4, the vorticity jump is

$$[\omega_r] = \frac{1}{h_1}\frac{\partial(u_2/M^2)}{\partial x_1} + M^2\frac{u_1}{u_2 h_1}\frac{\partial u_1}{\partial x_1} + M^2\frac{1}{u_2 h_1}\frac{\partial \Phi}{\partial x_1} + \left(\frac{1}{\rho u_2 h_1}\frac{\partial P}{\partial x_1}\right)_{\text{post}} - (\omega_r + 2\Omega_p).$$ (B5)

Assuming an locally isothermal equation of state $P = c_s^2 \rho$ gives $(P)_{\text{post}} = M^2 P$. The pressure term is then

$$\left(\frac{1}{\rho u_2 h_1}\frac{\partial P}{\partial x_1}\right)_{\text{post}} = \frac{1}{h_1(\rho u_2)_{\text{post}}}\frac{\partial(PM^2)}{\partial x_1}$$ (B6)

$$= \frac{c_s^2}{u_2 h_1}\frac{\partial M^2}{\partial x_1} + \frac{M^2}{\rho u_2 h_1}\frac{\partial P}{x_1},$$

where we have used the equation of state and $(\rho u_2)_{\text{post}} = \rho u_2$. Thus so far,

$$[\omega_r] = \frac{1}{h_1}\frac{\partial(u_2/M^2)}{\partial x_1} - (\omega_r + 2\Omega_p) + \frac{c_s^2}{u_2 h_1}\frac{\partial M^2}{\partial x_1} + M^2\left[\frac{u_1}{u_2 h_1}\frac{\partial u_1}{\partial x_1} + \frac{1}{\rho u_2 h_1}\frac{\partial P}{\partial x_1} + \frac{1}{u_2 h_1}\frac{\partial \Phi}{\partial x_1}\right].$$ (B7)

Using Eq. B3, terms in square brackets may be replaced with $\omega_r - \frac{1}{h_1}\frac{\partial u_2}{\partial x_1} + 2\Omega_p$ to give

$$[\omega_r] = \frac{1}{h_1}\frac{\partial}{\partial x_1}\left(\frac{u_2}{M^2}\right) + (M^2 - 1)(\omega_r + 2\Omega_p) + \frac{c_s^2}{u_2 h_1}\frac{\partial M^2}{\partial x_1} - \frac{M^2}{h_1}\frac{\partial u_2}{\partial x_1},$$

which may be simplified by noting that $\omega_r + 2\Omega_p = \omega$ is the absolute vorticity and $[\omega_r] = [\omega]$; using $u_2 = c_s M$ and $\frac{1}{h_1}\frac{\partial}{\partial x_1} = \frac{\partial}{\partial S}$ is derivative along the shock (i.e. S is the distance along the shock) to give

$$[\omega] = -\frac{c_s(M^2 - 1)^2}{M^2}\frac{\partial M}{\partial S} + (M^2 - 1)\omega - \frac{M^4 - 1}{M}\frac{\partial c_s}{\partial S}.$$ (B8)

This gives the vorticity jump across a shock using rotating frame velocities (and perpendicular to shock) but absolute vorticity on RHS.